The structure of epitaxial V_2O_3 films and their surfaces: a medium energy ion scattering study

A.J. Window, A. Hentz, D.C. Sheppard, G.S. Parkinson[1], D.P. Woodruff[2*]

Physics Department, University of Warwick, Coventry CV4 7AL, UK

W. Unterberger

Fritz-Haber Institut der MPG, Faradayweg 4-6, D 14195 Berlin, Germany

T.C.Q. Noakes, P. Bailey

STFC Daresbury Laboratory, Warrington WA4 4AD, UK

M.V. Ganduglia-Pirovano,

Institute of Catalysis and Petrochemistry – CSIC, Marie Curie 2, 28049 Madrid, Spain

……??

Abstract

Medium energy ion scattering (MEIS), using 100 keV H^+ incident ions, has been used to investigate the growth of epitaxial films, up to thicknesses of ~200 Å, of V_2O_3 on both Pd(111) and Au(111). Scattered-ion energy spectra provide a measure of the average film thickness and the variations in this thickness, and show that, with suitable annealing, the crystalline quality is good. Plots of the scattering yield as a function of scattering angle, so-called blocking curves, have been measured for two different incidence directions and have been used to determine the surface structure. Specifically, VEGAS simulations for a range of different model structures show poor agreement with experiment for half-metal (….V'O_3V) and vanadyl (….V'O_3V=O) terminations, with and without surface interlayer relaxations. However, good agreement with experiment is found for the modified oxygen-termination structure, first proposed by Kresse *et al.*, in which a subsurface V half-metal layer is moved up into the outermost V buckled metal layer to produce a VO_2 overlayer on the underlying V_2O_3, with an associated layer structure of ….O_3VV''V'O_3. This result is consistent with the predictions of thermodynamic equilibrium at the surface

[1] Present address: Institüt für Angewandte Physik, TU Wien, 1040 Wien, Austria

[2] Also at Fritz-Haber-Institut der MPG, Faradyweg 4-6, 14195 Berlin, Germany

[*] Corresponding author. Email d.p.woodruff@warwick.ac.uk

under the surface preparation conditions, but is at variance with the conclusions of earlier studies of this system that have favoured the vanadyl termination. The results of these previous studies are re-evaluated in the light of the new result.

Keywords: medium energy ion scattering (MEIS); surface structure; epitaxy; vanadium sesquioxide

1. Introduction

Oxide surfaces in general, and those of vanadium oxides in particular, play a major role in practical heterogeneous catalysis [1]. As such there have been many investigations of model oxide surfaces using surface science methods, but very few of these have involved quantitative surface structure determination. For many clean surfaces, including a number of oxide surfaces such as NiO(100) and rutile TiO_2(110), the structure differs from a simple bulk termination only by relatively small relaxations of atomic positions perpendicular to the surface. In the case of V_2O_3(0001), however, as for other corundum-phase structures (notably α-Al_2O_3 and Cr_2O_3), there are more fundamental questions to answer concerning not only such relaxations, but also at which of the several different atomic layers the bulk structure is terminated. It is also possible that the surface stoichiometry may differ from that of the underlying bulk in order to reduce the surface energy. Finally, we may ask whether, for these materials, the surface structure predicted to be in thermodynamic equilibrium with the gas phase under the preparation conditions of temperature and oxygen partial pressure is actually observed. In particular, previous studies of the (0001) faces of α-Al_2O_3 [2, 3, 4] and Cr_2O_3 [5, 6, 7, 8, 9] have indicated that is largely the case [10], but that for V_2O_3 it is not (e.g. [10, 11, 12, 13, 14, 15]).

Applying standard methods of UHV surface science to the surfaces of bulk oxide crystals leads, in many systems, to problems associated with charging (most oxides are insulators), and with *in situ* clean surface preparation (and re-preparation), due to the problems of defect creation and stoichiometry changes produced by incident ion bombardment. For this reason, an increasing number of studies of oxide surfaces have been conducted on thin epitaxial oxide films, generally grown on conducting (metal) substrates. Such films can be grown *in situ* in the UHV chamber, and can also be removed and regrown *in situ*, providing a means of repeated studies on consistent surfaces. Typically, these films are at most a few hundreds of atomic layers thick, and are commonly much thinner than this. In most cases characterisation of the films is by qualitative electron diffraction pattern observation (usually low energy electron diffraction – LEED) and/or scanning tunnelling microscopy (STM). Both techniques offer a way to characterise the surface order, but provide no direct information on the

underlying crystalline order.

Here we report the results of an investigation of V_2O_3(0001) films using the technique of medium energy ion scattering (MEIS), a method [16] that provides information on both the surface and deeper sub-surface crystallography. Our investigation was conducted on epitaxial films of the oxide grown *in situ* in the UHV analysis chamber on Au(111) and Pd(111) substrates. Previous studies [13] have shown that well-ordered V_2O_3(0001) films, as characterised by their low energy electron diffraction (LEED) pattern, can be grown on a range of substrates including Au(111) [12] and Pd(111) [17, 18, 19, 20, 21, 22], but also W(110) [12], Cu_3Au(100) [23, 24] and Rh(111) [25, 26, 27]. At room temperature the bulk structure of vanadium sesquioxide, V_2O_3, is trigonal (space group $R\bar{3}c$, no. 167) and can be represented by a hexagonal unit cell with lattice parameters of a=4.95 Å and c=14.00 Å containing six V_2O_3 units [28]. This value of a is a close match to the periodicity of the Au(111) and Pd(111) surfaces that have values of √3 times the nearest-neighbour distances of 4.99 and 4.76, respectively, corresponding to epitaxial mismatches of 0.8% and 3.8%. Relative to the (0001) basal plane, the structure of V_2O_3, like that of other corundum phases, comprises buckled layers containing 2 metal atoms per unit mesh alternating with planar layers containing 3 oxygen atoms per unit mesh; this layer structure is denoted here as ….O_3VV'O_3VV'O_3VV'….. (Fig. 1). The O layers are laterally distorted relative to a true close-packing, and the nearest V atoms occupy three-fold coordinated sites relative to these O atom layers.

Three distinct stoichiometric (0001)(1x1) terminations of this bulk structure can be envisaged, namely the oxygen termination …VV'O_3, and the full-metal termination ….O_3VV', (both being polar surfaces), and a half-metal layer termination with only one of the two vanadium layers being topmost, denoted as ….V'O_3V (Fig. 1). In this nomenclature the surface layer is on the right and the deeper bulk layers are on the left. One important variation of these surface terminations has O adatoms bonded atop the V atoms in the surface layer of the half-metal termination to produce a local vanadyl, V=O species; this structure may be denoted as …V'O_3V=O (Fig. 1). Detailed theoretical total-energy calculations based on density functional theory (DFT) have explored the surface relaxations to be expected for each of these terminations [11, 29, 30, 31] and the relative

energies have been evaluated as a function of the equilibrium oxygen chemical potential in the gas phase [11, 32, 33], generally favouring either a *partial* or zero vanadyl coverage of an otherwise oxygen-terminated surface under typical UHV surface preparation conditions. Experimental support for the presence of surface vanadyl species comes from vibrational spectroscopy; both HREELS (high-resolution electron-energy loss spectroscopy) [22] and infrared spectroscopy [12] have shown an adsorption band at ~130 meV that was attributed to a vanadyl V-O stretching mode. This has led to a general acceptance that the surface is *fully* covered with vanadyl species leading to a (1x1)-V=O termination. Near-edge X-ray absorption fine-structure (NEXAFS) spectra have been found to be consistent with theoretical simulations of the data for this fully vanadyl-covered termination model [34]. Most scanning tunnelling microscopy (STM) results have also been regarded as consistent with this termination, although a coexistence of the …VV'O_3 termination has also been proposed [20]. However, an investigation using the combination of low-energy noble gas impact-collision ion scattering spectroscopy with detection of neutrals (NICISS) and STM [24, 24] concluded that the outermost metal layer in the surface is a full VV' layer, rather than a V half-layer, and specifically excluded the presence of atop (vanadyl) O atoms; to reconcile this conclusion with the theoretically-predicted instability of a full-metal termination, partial coverage of near-bridging O atoms was proposed. The only published fully-quantitative structural study of this surface, using scanned-energy mode photoelectron diffraction (PhD), concluded that the surface does show a half-metal termination, but was unable to establish whether or not vanadyl O atoms were present [35]. A recent quantitative low energy electron diffraction (LEED) study, on the other hand, favours the fully-covered vanadyl termination model [36].

MEIS [16], typically using ~ 100 keV H^+ or He^+ incident ions, is a technique that can be used to explore true surface phenomena (occurring in the outermost one or two atomic layers of a solid), but also to investigate the sub-surface region up to thicknesses of a few hundred Ångström units. Scattered ion-energy spectra provide information on the depth-dependent elemental composition of ultra-thin films, because the energy of the scattered ions is determined by the atomic-mass-dependent recoil energy loss in the elastic ion-atom hard collision, and by the inelastic energy loss as the ions travel through the solid.

For a crystalline solid, elastic shadowing of sub-surface atoms by scattering from surface atoms restricts this information to the near-surface region if the ions are incident along a bulk crystallographic direction, but using a 'random' incidence direction deeper penetration and depth-profiling can be achieved. In addition, if the incident ion direction is chosen to illuminate only the near-surface layers through this incident-ion shadowing, the same physical process leads to 'blocking' of ions scattered from near-surface layers by the atoms lying closer to the surface. A measurement of the dependence of the scattered ion yield on the scattering angle (a 'blocking curve') to identify the directions of these blocking dips thus contains information on the relative positions of surface and near-surface atoms, providing a means to determine the structure of the outermost few atomic layers. Here we exploit both aspects of the technique to provide not only information on the stoichiometry, morphology and crystalline quality of the V_2O_3(0001) films, but also details of the surface termination and associated structural relaxations. A brief report of the main conclusions of this study regarding the surface termination, combined with a more quantitative analysis of the earlier NICISS study [23, 24], has recently been presented elsewhere [10], but here we provide a far more complete presentation of the results of the MEIS study of both the substrate and surface structure. We also present a detailed re-evaluation of earlier work, including the results of new STM image simulations.

2. Experimental details and initial sample characterisation

The experiments were performed at the Daresbury Laboratory UK National MEIS facility [37]. The ion accelerator, fitted with a duoplasmatron ion source, was used in the present experiments to produce a beam of H^+ ions at a nominal energy of 100 keV. Ions scattered from the sample were detected by a moveable toroidal electrostatic analyser, the two-dimensional (2D) detector [38] of which provides 'tiles' of ion counts as a function of both ion energy and scattering angle over limited ranges of each. The general methodology for extracting, from these raw data tiles, both the scattered-ion/energy spectra at fixed scattering angle and the angular blocking curves corresponding to scattering from a single atomic species, has been described elsewhere [37, 39]. The end-station comprises separate UHV chambers (typical pressures 2-5x10^{-10} mbar) for sample

preparation and characterisation, for sample storage, and for the ion scattering experiments, with sample transfer between chambers being achieved under UHV conditions. The Pd(111) and Au(111) samples were prepared *in situ* by the usual cycles of 1.5 keV argon ion bombardment (~10μA, 20 min) and annealing (to 600 °C for Au and 700°C for Pd) until well-ordered clean surfaces were obtained as judged by sharp (1x1) LEED patterns and the absence of contamination peaks in Auger electron spectra.

The V_2O_3 films were grown by V evaporation from an e-beam-heated rod tip in a partial pressure of oxygen. On Pd(111) the procedure used in another recent study [35] to produce ultra-thin films was followed, using a succession of doses of ~10 mins deposition in an oxygen partial pressure of $2x10^{-7}$ mbar with a sample temperature of ~300°C followed by heating to ~400°C for 1-2 mins after the oxygen had been pumped away. Typically 3 to 5 such doses were required to produce continuous films of average thickness 10-20 Å, as judged by the MEIS data. Initial tests using this procedure on the Au(111) substrate led to more heavily islanded films, with MEIS showing clear evidence of regions of exposed clean Au(111) surface. For this reason a modified procedure was used for growth on this substrate, following the method reported in an earlier characterisation of this growth system by Dupuis *et al.* [12]. In this case the same sample temperature and oxygen partial pressure was maintained during V deposition, but much longer deposition times of 1-3 hours were used, before the sample was annealed for 10-20 mins at 500°C in a reduced oxygen partial pressure of $5x10^{-8}$ mbar. This method led to significantly thicker films of up to ~200 Å. Blocking curves were recorded from all films, and showed very similar structure, but it is the blocking curves from one of these thickest films that form the basis of the surface structure determination reported here. All the films grown in this way showed a $(\sqrt{3}x\sqrt{3})R30°$ LEED pattern relative to that of the underlying Pd(111) or Au(111) surface, consistent with a $V_2O_3(0001)(1x1)$ surface. Note, though, that this LEED pattern (as is also clear from published patterns in previous studies) appears to have 6-fold rotational symmetry, rather than the 3-fold symmetry of both the fcc (111) substrate and $V_2O_3(0001)$. This effect can be attributed to the fact that the fcc(111) surface also has mirror symmetry (space group p3m) which is lacking in V_2O_3, leading to two inequivalent domains of the overlayer film related by a 180°

rotation about the surface normal; the equal occupation of these symmetrically-equivalent domains leads to the increased symmetry of the diffraction pattern.

One feature of the MEIS technique that proves to be important in its use for surface structure determination is the ability to quantify the scattered ion yields in terms of the number of contributing atomic layers. To achieve this the scattered ion yields were calibrated using measurements from a reference sample of Cu shallowly implanted in Si to a known concentration (3.12×10^{15} atoms.cm^{-2} with a precision of ±3%), established independently by conventional Rutherford backscattering. Past experience indicates that this method of calibration provides yields from the sample under study that are accurate to better than 10%.

In any technique involving incident energetic ion beams, it is clearly important to assess the scale of possible sample damage resulting from the ion impact. While 100 keV H^+ or He^+ ions clearly do cause damage to any surface, through elastic recoil of the surface atoms that scatter the incident ions, the general mode of use of MEIS ensures that the total number of incident ions used in collecting the data is small enough that there is a low probability that a second ion will scatter from exactly the same atomic position. Nevertheless, potentially more serious issues arise in an oxide surface. One such problem is the effect of atomic mixing, due to recoil scattering and the subsequent collision cascade. A further potential source of damage (atomic displacements, vacancy creation) in oxides is through electronic excitations. In order to assess the scale of possible radiation damage in the present case, a series of MEIS scattered ion energy spectra were measured from V_2O_3 films around the V scattering peak, keeping the incident beam (directed along a bulk crystallographic direction to ensure surface specificity) in the same position on the sample. Damage may be expected to manifest itself in: (i) a broadening of the low-energy side of the V scattering peak due to subsurface displacements of V atoms from their equilibrium positions in the crystalline oxide; (ii) an increase in the background under the V peak corresponding to similar displacement of atoms in the underlying substrate. This second effect will only occur if the scattering peak from the substrate occurs at higher energy than that of the V. Both Pd and Au have a higher atomic mass than that of V, and so lead to higher scattered ion energies than from V when these

atoms are at the surface. However, these substrate scattering peaks are displaced down in energy as the oxide overlayer becomes thicker due to increasing inelastic energy loss (e.g. Fig. 2), so for thicker films the scattered ions from the substrate can emerge at a lower energy than those scattered from surface V atoms. A damage-test experiment on a film grown on Au(111) showed no change in the V scattering peak shape for integrated incident ion dose up to 100 μC, although a very small increase in background yield was detectable with a total ion dose at the sample in excess of 16 μC, corresponding to ~$2x10^{14}$ ions/mm^2. This background signal increased further with increasing incident ion dose. The implication is that even the much higher total flux produces no significant displacement of V atoms in the oxide, and the effect detected actually corresponds to displacement damage in the underlying metal. This seems to be confirmed by a similar test on a V_2O_3 film on Pd(111) which showed no spectral change up to a total ion dose of 100 μC. Nevertheless, in recording the MEIS data presented here, care was taken to ensure that no region of the surface was exposed to a total incident ion beam dose of more than 16 μC. A more stringent test of radiation damage would, in principle, be provided by a similar test on the O scattering peak. Unfortunately, this proved not to be possible because of the much lower scattering cross-section; as such, reasonable statistics in this scattering peak are only be achievable with very much higher ion doses than the probable damage threshold.

3. Results

3.1 Scattered-ion/energy spectra

Fig. 2 shows representative scattered-ion energy spectra recorded from several films grown on the two different substrates. In each spectrum the three peaks, associated with scattering from the V and O atoms of the film, and the Pd or Au atom of the substrate, are identified. The average film thicknesses, *t*, as determined from these MEIS spectra (see below) are noted on the figures. All spectra were recorded using incident and collection directions that correspond to bulk crystallographic directions of the metallic substrates; this 'double alignment' [16] geometry leads to a substrate scattering signal that only contains contributions from the outermost layers of the substrate; for this reason the scattering peaks from the substrate are generally narrow, because there is no contribution to scattering from deeper layers that would suffer significant inelastic loss. The specific

geometries used were $[\bar{1}\bar{1}0]$ incidence and [112] detection for the measurements on Pd(111), and $[00\bar{1}]$ incidence and [111] detection for those on Au(111); these two geometries have the same scattering angle of 125.3°, and are shown schematically in Fig. 3. The epitaxial relationship corresponds to the (0001) face of the oxide being parallel to the (111) face of the substrate, while the $[2\bar{1}\bar{1}0]$ direction of the oxide within the interface plane is parallel to the $[1\bar{1}\bar{2}]$ direction of the substrate. An important consequence of this relationship is that these substrate incident shadowing directions are almost exactly coincident (to within ~0.1°) with crystallographic directions in the oxide. Specifically, the substrate $[\bar{1}\bar{1}0]$ direction is parallel to $[\bar{4}22\bar{3}]$ in the oxide, while the substrate $[00\bar{1}]$ direction is parallel to $[8\bar{4}\bar{4}3]$ in the oxide. Good crystalline epitaxy should therefore lead to narrow MEIS peaks from *both* the substrate and film scattering in these geometries, and this is seen in the experimental data.

One characteristic feature of the scattered-ion energy spectra of Fig. 2 is the increasing shift to lower energy of the scattering peaks from the substrate Pd and Au atoms as the film becomes thicker. As remarked above, this is a consequence of the inelastic energy loss suffered by the ions in passing through the oxide film; this shift, combined with an absence of any similar shift for the scattering peak from V, shows that the V_2O_3 is growing on top of the metal surfaces. The spectra in the upper right-hand panel of Fig. 2, recorded from a 50 Å film of V_2O_3 on Au(111), show the effect of annealing the film after the initial deposition. The spectrum from the unannealed film shows a broad peak associated with scattering from V atoms, because the V_2O_3 film is poorly ordered, so V atoms throughout the film at different depths (with different amounts of inelastic scattering) contribute to the peak. Annealing the film, however, leads to good crystalline order and the scattering is now only from the outermost surface of the oxide, leading to a much narrower peak at the highest energies. Notice that annealing also leads to some (much weaker) narrowing of the Au scattering peak. This probably arises because the ion passage through the disordered oxide leads to 'dechannelling' of the incident ions, scattering ions out of the crystallographic incidence direction, and allowing subsurface Au atoms to become visible to the ion beam. Annealing also leads to a small shift in the

Au scattering peak to lower energy, attributable to a spreading of the inhomogeneous islanded film, such that areas of the surface with a very thin covering of oxide are covered more thickly; this leads to more energy loss in ions scattered from the interface Au atoms in these regions. The substantially broader scattering peak from Au when the substrate in covered with a much thicker (200 Å) oxide film (bottom right-hand panel of Fig. 2), is a consequence of ion straggling, as well as dechannelling and variations in the film thickness.

More quantitative information can be obtained from these spectra using the SIMNRA program [40], and superimposed on the raw experimental data points of Fig. 2 are full lines derived from simulations using this software. The rate of inelastic energy loss in the oxide film (the 'stopping power') was obtained using SRIM [41]. Two important pieces of information can be obtained from these simulations. The first derives from the fact that the calculations were based on the assumption that the oxide stoichiometry V:O was 2:3, as expected for V_2O_3. If this value is correct the O scattering peaks should be identical to the V scattering peaks except that they are offset in energy by the different recoil energy loss, and modified in intensity by the different scattering cross-section (and the assumed relative stoichiometry). Although the scattering signal from the O atoms is weak, it is clear that these assumptions lead to good fits to the data, confirming the stoichiometry of the oxide film. The second piece of information, obtained from the parameters used in the simulations, is the average film thickness and the variation in this thickness; these parameters determine the energy and shape of the substrate scattering peaks. These values are summarised in Table 1 for several different preparations. For the thinnest films, mainly prepared on the Pd(111) substrate, there is a large variation in the film thickness that we attribute to island growth. When the sequential short dose/anneal method used for the films on Pd(111) was applied to the Au(111) substrate, the MEIS spectra from the resulting thin films clearly showed evidence of areas of the surface on which the bare Au(111) substrate was exposed, indicating a Volmer-Weber, rather than Stranski-Krastenov, growth mechanism, as remarked above. Longer deposition times prior to annealing appeared to achieve films of more-nearly homogenous thickness.

3.2 Blocking curves

MEIS can provide rather detailed crystallographic information through the use of 'blocking curves' – measurements of the scattered-ion signal from a particular atomic species in the near-surface region as a function of scattering angle. These blocking curves can be simulated for a specific model structure using the VEGAS computer program [42]. Structure determination can then be achieved by a 'trial-and-error' process of testing different models with different structural parameter values until the best fit with experiment is achieved. An objective measure of the quality of this agreement between experiment and theory is provided by a reliability- or *R*-factor [43, 44] defined as

$$R = \left(\frac{1}{N}\right)\sum_{i}^{N}\left[\frac{(I_{\exp} - \lambda I_{theo})^2}{I_{\exp}}\right]$$

Where N is the number of data points in the blocking curve(s), $I_{\exp}$ and I_{theo} are the experimental and theoretically simulated ion yields, and λ is the calibration scaling factor obtained, in the present case, from the reference sample as described in section 2. In the standard form of this *R*-factor, the experimental ion yields are expressed in terms of raw ion counts, an approach that allows one to use standard statistical methods to estimate the errors in the resulting structure determination. However, in this form the *R*-factor is dominated by the much higher count rates recorded at small scattering angles, θ, because the scattering cross-sections scale as $\text{cosec}^4(\theta)$. In presenting experimental and theoretical blocking curves for visual comparison, the raw data are corrected for this angular dependence to allow, after determination of the calibration factor, λ, the yields to be presented in terms of the number of visible (contributing) layers of scattering atoms. Specifically, the V scattering yields presented here are in terms of the number of V atoms within a complete V_2O_3 layer – i.e. the number of V atoms in a combined buckled VV' layer. In order to ensure that *R*-factor accurately reflects the visual appearance of these comparisons, and weights the full angular range of the data equally, the values reported in this paper are of an *R*-factor in which the *I* values are the ion yields in terms of layers, and not the raw measured ion counts.

In order to investigate the surface structure of the $V_2O_3(0001)$ films, blocking curves of

the V scattering yield were measured for two incidence geometries, namely the $[8\bar{4}\bar{4}3]$ direction in the $[2\bar{1}\bar{1}0]$ azimuth, and the $[20\bar{2}\bar{1}]$ direction in the $[10\bar{1}\bar{0}]$ azimuth. These azimuthal directions are shown in a top view of the bulk structure in Fig. 4. Both of these incident directions also correspond to bulk crystal directions in the underlying metal substrate, specifically, $[8\bar{4}\bar{4}3]$ is parallel to $[00\bar{1}]$ in the substrate, as noted above, and $[20\bar{2}\bar{1}]$ is parallel to $[1\bar{5}\bar{2}]$ in the substrate. Figures 5 and 6 show the side view of the atomic scattering planes in these two azimuths. As may be seen from Fig. 4, in the $[10\bar{1}\bar{0}]$ azimuth the O atoms of the bulk lie far from the scattering planes of V atoms, so no shadowing or blocking is to be expected of the ions scattered from the V atoms by these O atoms. However, vanadyl O atoms, if present, can produce both shadowing and blocking, and are shown in the side view of the scattering planes. There are two inequivalent (laterally-displaced) scattering planes in this azimuth that make up the structure, and these are shown in different colours in the figure. Shadowing and blocking of atoms of one colour can only occur at other atoms of the same colour (and thus in the same plane of atoms). For the $[10\bar{1}\bar{0}]$ azimuth, an added complication is that two inequivalent domains exist, related by a rotation of 180° (or, equivalently, 60°) due to the higher substrate symmetry, as discussed earlier. This second type of domain is also shown in Fig. 5. In the case of the $[2\bar{1}\bar{1}0]$ azimuth, there are four distinct, laterally-displaced scattering planes of atoms, shown in four different colours in Fig. 6. In this azimuth the O atoms of the bulk are also not exactly within the V atom planes (see Fig. 4), but they are sufficiently close to these planes that some shadowing and blocking can occur, so these atoms are included in Fig. 6. As the $[2\bar{1}\bar{1}0]$ direction lies perpendicular to a mirror plane of the substrate crystal, the structures of the different rotational domains are all equivalent in this azimuth.

Fig. 7 shows the experimental blocking curves obtained in these two incidence geometries from a 200 Å thick V_2O_3 film grown on Au(111); this is the same film for which the double-alignment scattered-ion energy spectrum is shown in the bottom right-hand corner of Fig. 2. Closely similar blocking curves were measured for many films of sufficient thickness grown on both Au(111) and Pd(111), but the dataset shown in Fig. 7

appears to be the best in terms of ion statistics and film quality (as judged by both the narrow V peak in the scattered-ion energy spectrum and the clarity of dips in the blocking curves). For $[20\overline{2}1]$ incidence, the main crystallographic bulk blocking directions identified in Fig. 5 are indicated, and clearly correspond quite well to dips seen in the experimental data. Simulations of these blocking curves were then performed using the VEGAS program for the full metal, half-metal and vanadyl termination models, taking the structural parameter values (notably the interlayer relaxations) from the published theoretical and experimental structural investigations. These are the three models of the ordered (1x1) surface that have attracted the most attention in previous experimental studies of this surface. The structural parameter values of these different models are summarised in Table 2. For each of the three terminations, a reference model is included with no interlayer relaxations relative to the bulk values, while other models include the values of the relaxations found in the theoretical calculations of Czekaj, Herman and Witko (CHW) [29] and Kresse, Surnev, Schiswohl and Netzer (KSSN) [11], and in the experimental PhD study of Kröger, Sayago, Allegretti *et al.* (KSA+) [35]. Additional test models were created by removing the vanadyl O atoms from one vanadyl model to create a half-metal model, and adding a vanadyl O to half-metal models (at a V=O distance of 1.61 Å) to produce vanadyl models. An example of the quality of the agreement between theory and experiment is provided by the full lines in Fig. 7, that correspond to the simulations for the half-metal and vanadyl termination models obtained in the KSA+ PhD experiments. Based on the low *R*-factor values of Table 2, these two models are amongst those providing the best agreement between theory and experiment. Inspection of Fig. 7, however, shows that in several angular ranges of the two blocking curves the level of agreement is actually poor. The fact that the *R*-factor values for most of the other structural models are higher is consistent with similar visual inspection of their associated simulations that shows that these, too, yield poor fits to the experimental data, with the discrepancies shown in Fig. 7 being typical of the whole set.

One interesting feature evident in the data recorded in $[20\overline{2}1]$ incidence is that the dominant blocking dips occur at the angles anticipated by simple considerations of the bulk structure (as in Fig. 5), yet the theoretical simulations for the different surface

termination models fail to reproduce the shape or magnitude of these blocking dips. Indeed, it is notable in Table 2 that both the *R*-factor value for the $[20\overline{2}1]$ incidence data, and that for both data sets combined, are also low for the simulations for the double-metal termination with bulk-like interlayer spacings. The implication of this is that a simulation of the *bulk* blocking pattern might actually fit the data better than these simulations of the *surface* blocking. On the other hand, the narrow V scattering peak in the scattered-ion energy spectra, and the generally good fit of the surface simulations to the absolute scattering yield, makes it clear that the experimental data do correspond to surface, rather than subsurface (bulk) scattering. One possible solution to this dilemma could be that the ion incidence direction is slightly misaligned relative to the proper bulk crystallographic shadowing direction. While the consistency of the experimental blocking curves over many different experiments, performed at different times and on different sample preparations, makes it unlikely that such an error would arise consistently from experimental misalignment, small variations in alignment could be an intrinsic feature of the epitaxial films that might contain small-angle grain boundaries. This would lead to some enhanced illumination of sub-surface atoms, and the scattering from these deeper layers is expected to show a bulk blocking pattern. Notice, though, that a large misalignment will lead to a greatly increased average scattering yield that is incompatible with the experimental yields.

Fig. 8 shows the results of simulations, designed to explore this effect, that show the effect of a 1° misalignment of the incidence directions. Simulations are shown for both the half-metal and vanadyl terminations based on the bulk interlayer spacings. In addition, simulations are shown for one set of representative layer spacings that include the main effect of surface relaxation seen in the various theoretical and experimental investigations included in Table 2, namely a contraction of the outermost V_{top}-O_{top} layer spacing of ~30% to a value of 0.68 Å. These simulations do yield a significant improvement in the fit to experiment, with values of the *R*-factors for the relaxed vanadyl structure being $R[20\overline{2}1]=0.06$, $R\ [8\overline{4}\overline{4}3]=0.24$, R (total) $=0.16$. However, despite this reduction in *R*, visual inspection shows that there remain many significant discrepancies between experiment and theory.

The one termination of Fig. 1 which was not explored in these initial simulations is the pure oxygen, ….VV'O_3 model, mainly because this has not generally been considered favourable and, in the form shown in Fig. 1, should be highly polar and thus unstable. However, KSSN [11] reported that in their DFT calculations, if this structure is allowed to relax to its lowest energy configuration, the second half-metal layer of V_2 atoms moves up into the outermost buckled $V'_{top}V_{top}$ layer (Fig. 1), such as to produce a non-polar V_3O_6 (i.e VO_2) compound layer, as shown in Fig. 9. The structure of this outermost triple $O_3V_3O_3$ layer is very similar to that of bulk VO_2. This effect was also reproduced in the DFT calculations of Todorova, Ganduglia-Pirovano, and Sauer (TG-PS) for an epitaxial film of V_2O_3 on α-Al_2O_3(0001) [32], while both studies indicate that this structure may be the most favoured structure energetically under typical UHV preparation conditions. We have relabelled the displaced V'_2 layer as V''_{top} and henceforth refer to this as the KSSN ..O_3VV''V'O_3 model, or the VO_2 termination. Our MEIS simulations were therefore extended to include this model, and some minor adjustments of interlayer spacings were explored to find values that optimised the theory/experiment agreement. The results of these simulations are shown in Fig. 10, while Table 3 lists the interlayer spacings found for this model and compares them with the values of the original KSSN [11] theoretical study, together with values for the best-fit previously-proposed structure (the half-metal termination from the experimental PhD study [35]) and the best-fit previously-proposed structure including the effects of a 1° misalignment (a relaxed vanadyl termination model). The *R*-factor values for the VO_2-termination structure are $R[20\overline{2}1]$=0.03, R $[8\overline{4}\overline{4}3]$=0.16, R (total) =0.10; these values are all significantly lower than those obtained from any of the other structures, even after including the effects of possible misalignments, and this is consistent with visual inspection (Fig. 10) that clearly shows a very good level of theory/experiment agreement. We therefore conclude, on the basis of experimental MEIS blocking curves, that the V_2O_3(0001) films grown in this study do have this KSSN ..O_3VV''V'O_3 termination; the optimised interlayer spacings (Table 3) are closely similar to those found in the DFT calculations [11].

4. Photoelectron diffraction revisited

While our MEIS study (and the parallel NICISS study [10]) provides strong evidence for the KSSN ..O_3VV''V'O_3 termination model for the V_2O_3(0001) surface of our films grown on Au(111) and Pd(111) to thicknesses of ~200 Å, this conclusion is at variance with the only previous experimental studies of the surfaces of films prepared in a closely similar way. In particular, the PhD study [35] performed by our own group, the only previously-published quantitative structure determination, concluded that the surface has a half-metal termination, although the presence or otherwise of adsorbed oxygen, to produce surface vanadyl species, was unresolved. This earlier investigation, however, did not consider the KSSN ..O_3VV''V'O_3 termination model. We have therefore undertaken new PhD simulations of this structure to establish whether an acceptable level of theory/experiment agreement can be achieved for this structural model. The calculations were performed using exactly the same simulation codes and methodology as in the original publication [35], which provides full details.

Fig. 12 shows the results of these new calculations, compared with those of the original publication, and of the experiments. The experimental data comprise O 1s and V 2p scanned-energy mode photoelectron diffraction modulation spectra recorded at a range of different emission directions (the azimuths and polar angles are specified in the figure), and these are compared with the results of simulations for the original geometrically-optimised half-metal terminated structure, and for the VO_2-terminated structure found to give the best fit to the MEIS data. The level of theory-experiment agreement for the original PhD structure determination is quite good for the V 2p spectra, but less good for the O 1s spectra; some of the difficulties associated with applying the PhD technique to this surface, using photoemission signals that result from both the surface and the underlying substrate, have been discussed previously [35]. For the MEIS model of the VO_2-terminated structure, the agreement with experiment is clearly very much worse, especially for the V 2p emission. We must conclude, therefore, that the PhD data are *not* consistent with this structure. Of course, two distinct techniques may be expected to lead to slightly different optimised values of the structural parameters, but attempts to make minor adjustments to these values given by the MEIS analysis failed to identify any

closely-related structure that gave a significantly better fit to the PhD data. One modification that did yield a substantial improvement, particularly for the V 2p spectra, was to allow the V'' layer to move back down into the substrate towards (but still far from) its bulk-terminated location by some 0.5 Å. This model gave an overall PhD *R*-factor almost identical to that for the originally-favoured half-metal (or vanadyl) termination, and the results of the associated simulation are also shown in Fig. 12; the fit to the O 1s spectra is slightly better, that to the V 2p spectra slightly worse. However, MEIS simulations using this modified geometry yielded much worse *R*-factors, primarily because the displaced V atom leads to a significant increase in the absolute scattering yield that is inconsistent with the experimental data. Of course, as we remarked above, this absolute yield calibration is subject to some error. If this calibration is changed by 13%, the new PhD model is found to yield MEIS *R*-factors that are very close to those of the preferred MEIS model, although visual inspection shows the fit of some of the blocking features to be somewhat worse (Fig. 12). A calibration error of 13% is, however, somewhat larger than previous experience in the study of other systems that puts an upper limit on this error of 10%.

We must therefore conclude that neither the half-metal termination, nor the KSSN VO_2 termination, can be fully reconciled with both experimental data sets, although this modification of the VO_2 termination model might offer an acceptable solution. However, we also note that simulations of LEED intensity-energy spectra for the VO_2-termination model indicate that this structure is not compatible with previously-recorded [36] quantitative LEED data, although exhaustive searches of the structural parameter values have not been undertaken [45].

5. General discussion

Our MEIS study provides strong evidence for the KSSN ..O_3VV''V'O_3 termination model of the V_2O_3(0001) surface on our films grown on Au(111) and Pd(111) surface to thicknesses of ~200 Å, and we note that a quantitative analysis of NICISS data also provides clear support for this model in preference to the half-metal or vanadyl terminations [10]. Moreover, a very recent independent investigation exploiting the

structure-dependence of electron emission induced by fast H atom scattering at very grazing angles [46] has also concluded that the data are consistent with the VO_2 termination model and not with a vanadyl termination. Nevertheless, this conclusion is at variance with those of a large body of previous experimental work, although the only previous fully-quantitative structural studies are those by PhD and LEED, discussed above.

Before considering how our conclusions might be reconciled with this additional experimental evidence, however, we first address the findings of two DFT investigations of the surface phases expected to be in thermodynamic equilibrium with the gas phase under the conditions of temperature and oxygen partial pressure relevant to the experimental surface preparations. Fig. 13 shows a calculated phase diagram, adapted from the calculations of TG-PS [32, 33], showing the surface terminations expected as a function of the oxygen and vanadium chemical potentials relative to gas-phase O_2 and metallic bcc bulk V, respectively. These calculations were performed for an epitaxial film of V_2O_3 (three complete V_2O_3 layers thick) on α-$Al_2O_3(0001)$, and the grey-hatched region covering much of the left-hand side of the diagram corresponds to conditions under which the clean underlying alumina substrate is more stable that the film (i.e the equilibrium film thickness is zero). The bold diagonal line defines the condition for equilibrium of the film with bulk V_2O_3 which occurs when

$$2\mu_V + 3\mu_O = E_{tot}(V_2O_3)$$

or, using the relative chemical potentials used in Fig. 13,

$$2\Delta\mu_V + 3\Delta\mu_O = E_{tot}(V_2O_3) - 2E_{tot}(V_{bulk}) - (3/2)E_{tot}(O_2) = -11.784 \text{ eV}$$

The intersections of this bold line with the phase boundaries thus define the limits of the different surface phases that are calculated to be in equilibrium with bulk V_2O_3 and with oxygen in the gas phase at the relevant relative oxygen chemical potentials. These intersections, marked with vertical grey lines, are projected down onto the resulting simplified diagram at the bottom, which also shows corresponding oxygen partial pressure values for two different temperatures. Very similar results were presented in the earlier paper of KSSN [19] who considered only the influence of the oxygen chemical potential assuming equilibrium with bulk V_2O_3. The exact values of relative oxygen chemical potential corresponding to the phase boundaries differ slightly in the TG-PS and

KSSN calculations, and may probably be regarded as an indication of potential imprecision in these locations; the differences in these specific calculations may arise from a number of factors including the inclusion (TG-PS) or neglect (KSSN) of spin polarisation and the fact that KSSN used double-sided free-standing V_2O_3 slabs with the middle layers constrained to the bulk structure, whereas TG-PS use single-sided slabs of V_2O_3 epitaxial on thin α-Al_2O_3 slabs (with a 4% lattice mismatch). In both cases, however, the generalized gradient functional of Perdew and Wang (PW91) [47] was used. Here, it is important to mention that the PW91 gradient approximation tendency to overestimate formation and binding energies means that the oxygen chemical potential ($\Delta\mu_O$) might be shifted by several 100 meV. Thus, the absolute pressures might be in error by 2 to 3 orders of magnitude. Nevertheless, the general stability trend is valid, and what is clear from Fig. 13 is that typical film growth and surface annealing conditions correspond to the oxygen chemical potential range of the boundary between the equilibrium surface phases of the VO_2 termination ($\ldots O_3VV''V'O_3$) and an O_3 termination with a partial (1/3 ML) coverage of vanadyl species ($\ldots O_3VV''_{2/3}V'O_3(V{=}O)_{1/3}$). Notice that in the partially vanadyl-covered surface the V'' atom of the VO_2 termination that lies below the surface vanadyl species shifts back down into the second bulked vanadium layer. One other important feature of Fig. 13 is to note that there is *no* value of the relative oxygen chemical potential that is predicted to lead in equilibrium to pure (1x1) vanadyl, or pure half-metal, terminated surfaces. Indeed, the extreme left of the simplified surface phase diagram (where partial half-metal terminations are predicted) corresponds to negative (and thus physically meaningless) values of the vanadium chemical potential.

A key conclusion from these theoretical calculations is thus that the VO_2 termination favoured in our MEIS study is broadly consistent with a predicted equilibrium structure, but a (1x1) vanadyl termination is not, under *any* preparation conditions. Of course, an obvious question is whether any of these experiments do achieve the necessary equilibrium. In this regard, however, we note that the experimentally-observed terminations of α-$Al_2O_3(0001)$ and $Cr_2O_3(0001)$, with several studies being performed on the surfaces of bulk oxide crystals, are broadly consistent with comparable theoretical predictions of equilibrium surface phases [10]. Film growth is, of course, intrinsically a

non-equilibrium process, yet one might anticipate that slow growth (typically significantly less than 1 Å/min) under well-defined conditions of oxygen pressure and temperature may provide and easier route to achieve equilibrium that any treatment of the surface of a bulk crystal.

Despite this theoretical support, and the apparently consistency of our findings with results for other corundum-phase surfaces, there is a body of evidence that has been taken to support the alternative view that the $V_2O_3(0001)$ surface is vanadyl-terminated. The clearest evidence of the presence of vanadyl terminations is the observation in vibrational spectroscopies of an absorption band consistent with a vanadyl stretching vibration [12, 22]. This is not, however, inconsistent with the phase diagram of Fig. 13, in that structures with *partial* vanadyl coverage are predicted to occur in the range of oxygen chemical potentials relevant to the preparation conditions of these films. Vibrational spectroscopies do not allow one to estimate the coverage of any species giving rise to an absorption band, and indeed a V=O coverage of ~0.1 ML would have little effect on our MEIS (or the NICISS) data. In this regard we note that DFT slab calculations can only be performed on periodic structures, and the possibility of partial V=O coverage has only been explored using the values of 0.33 ML and 0.67 ML corresponding to one or two V=O species per $(\sqrt{3}x\sqrt{3})R30°$ unit mesh; it is possible that even lower coverages may be even more stable. For this reason, the observation of a (1x1) LEED pattern need not conflict with these conclusions; LEED provides information on the average long-range order, and indeed the observed patterns are dominated by those regions (which may be a minority of the surface) that are well-ordered.

However, experimentally-obtained STM images showing (1x1) ordered surfaces with a single circular atomic-scale protrusion per unit mesh in STM (e.g. [20, 24, 48]) have been generally regarded as consistent with a (1x1) vanadyl termination. The fact that the oxygen-terminated surface contains three O atoms per (1x1) surface unit mesh would lead one to expect STM images that show more than one such protrusion within the unit mesh; previous STM simulations of the vanadyl-terminated surface do show a single protrusion in each unit mesh [20] consistent with the usually expected termination, but simulations of a bulk-type oxygen-terminated surface also show a single protrusion,

albeit with a triangular shape [20]. Our own simulated empty-state images of these two surfaces, and of the VO_2 termination, are shown in Fig. 14. These simulated images were generated within the Tersoff-Hamman approximation, the V_2O_3(0001) surface being modelled by a supercell with six complete V_2O_3 layers using the previously optimized bulk lattice constants [32]. The spin-polarized DFT-PW91 calculations were performed with an energy cut-off of 400 eV and a (6x6x1) *k*-point grid for the (1x1) hexagonal surface unit cell, with other computational details as previously reported [32]. The results for the vanadyl and bulk O_3 terminations are closely similar to those previously presented by Surnev *et al.* [20], although the three surface O atoms are more clearly resolved in Fig. 14. The simulations for the VO_2 termination are similar to that of the bulk O_3 termination, with clearly resolved features attributable to the three surface O atoms per surface unit mesh. Of course, it is important to recognise that the exact appearance of simulated images depends on the exact charge-density contours that are mapped, and the degree of resolution in a real instrument can also vary. Perhaps more significantly, important variations in the atomic-scale images from the V_2O_3(0001) surface have been reported both as a function of imaging conditions (notably variation of the bias voltage at fixed tunnelling current [24]) and in coexistent surface regions at fixed imaging conditions [20]. In particular, images that show significant structure within the unit mesh have been reported (e.g. Fig. 4 of ref. [24]) that may be more compatible with those predicted for the VO_2 termination.

One feature of the as-prepared V_2O_3(0001) surface is that it is chemically inactive, with no evidence of strong chemisorption of any adsorbates. This has been attributed to oxygen termination in the form of vanadyl species, and electron-beam irradiation, believed to cause oxygen desorption, is found to lead to greatly enhanced surface reactivity (e.g. [48, 49, 50]) this observation is certainly consistent with O removal from surface vanadyl species to expose a half-metal termination, but could also be consistent with the removal of O atoms from a VO_2-terminated surface, which would similarly expose underlying and potentially more reactive V atom sites. In this regard, the conclusions of a PhD study [51] of the effect of exposing the as-prepared surface to atomic hydrogen is also significant; as expected, this leads to the creation of surface hydroxyl species, but the PhD results show that these hydroxylated O atoms are not in the

atop sites of a V=O species, but occupy the sites of the outermost O_3 layer.

6. Conclusions

Our MEIS study of the growth of V_2O_3(0001) films on Pd(111) and Au(111) confirms that good epitaxial and stoichiometric well-ordered films with thicknesses of up to ~200 Å can be obtained using standard procedures developed in the past and described in earlier literature. Comparison of experimental MEIS blocking curves with simulations for a range of structural models of the surface termination, does not, however, support the currently-held conventional wisdom of recent publications that the surface comprises a (1x1) ordered half-metal termination that is capped with O atoms to produce a surface layer of vanadyl, V=O, species. Instead, good agreement is found for a relaxed oxygen-terminated surface with an outermost VO_2 trilayer. This structure is consistent with the results of previous DFT calculations that are based on the *equilibrium* structure in contact with gas-phase oxygen in the partial pressure and temperature range broadly consistent with the film growth conditions. It is also consistent with a recently-published quantitative analysis of NICISS data [10], and the results of electron emission by fast atom interaction [46]. Possible reasons for the apparent inconsistency of this conclusion with the results of previous experimental studies by other methods have been discussed; reinterpretation of much of the previous information in terms of the predicted equilibrium surface phases appears to be possible, although some remaining inconsistencies, notably with earlier PhD and LEED results, are as yet unreconciled.

Acknowledgements

The authors acknowledge the financial support of the Engineering and Physical Sciences Research Council (UK), and of the Deutsche Forschungsgemeinschaft through the Sonderforschungsbereich 546. MVGP thanks the SGAI-CSIC (Secretaria General Adjunta de Informática–Consejo Superior de Investigaciones Científicas) for computational resources.

Table 1

Summary of film thickness information extracted from simulations of the scattered-ion energy spectra (e.g. Fig. 2) using SIMNRA. Note that the dosing procedures used on the two substrates differed, as described in the text.

substrate	preparation	Average thickness, *t* (Å)	Variation in thickness (Å)
Pd(111)	1x 10 min dose	1.3	1
	2 x 10 min doses	5.4	3
	3 x 10 min doses	7.7	4
	4 x 10 min doses	11	7
	5 x 10 min doses	20	11
	2 hr deposition	190	40
Au(111)	40 min deposition	50	16
	3 hr deposition	200	16

Table 2. Summary of the initial structural models tested in the VEGAS simulations of the MEIS blocking curves, together with the associated values of the *R*-factor providing a measure of the quality of agreement with experiment. The spacings between layers (as labelled in Fig. 1) are in Ångström units. The relevant citations for previously-proposed structures are CHW [29], KSSN [11], KSA+ [35].

basic model	half-metal (HM) …V'OV					vanadyl …….V'OV=O					full metal ..OVV'
Parameter	bulk	CHW	CHW V=O minus O	KSSN	KSA+	bulk HM + O	CHW HM + O	CHW	KSSN	KSA+	bulk
$R[20\overline{2}\overline{1}]$	0.06	0.19	0.07	0.31	0.13	0.09	0.16	0.06	0.03	0.07	0.06
R $[8\overline{4}\overline{4}3]$	0.95	0.32	0.46	0.40	0.36	1.1	0.44	0.58	0.95	0.58	0.61
R (total)	0.56	0.26	0.29	0.36	0.26	0.64	0.32	0.35	0.54	0.35	0.37
V_{top}-V'	-	-	-	-	-	-	-	-	-	-	0.36
V_{top}=O	-	-	-	-	-	1.61	1.61	1.59	1.61	1.55	-
O_{top}-V_{top}	0.98	0.68	0.82	0.35	0.68	0.98	0.68	0.82	0.75	0.69	0.98
V'_{top}-V_{top}	0.98	0.98	0.93	1.12	0.93	0.98	0.97	0.93	0.99	1.05	0.98
V_2-$V_{t'op}$	0.36	0.27	0.34	0.22	0.35	0.36	0.27	0.34	0.28	0.34	0.36
O_2-V_2	0.98	0.96	0.96	1.13	1.02	0.98	0.96	0.96	1.08	0.95	0.98
V'_2-O_2	0.98	0.98	0.98	1.02	0.98	0.98	0.98	0.98	0.99	0.98	0.98
V_3-V'_2	0.36	0.36	0.36	0.38	0.36	0.36	0.36	0.36	0.41	0.36	0.36
O_3-V_3	0.98	0.98	0.98	1.01	0.98	0.98	0.98	0.98	1.00	0.98	0.98
V'_3-O_3	0.98	0.98	0.98	0.98	0.98	0.98	0.98	0.98	0.98	0.98	0.98

Table 3. Interlayer spacings (as labelled in Fig.9) for the originally-proposed [11] KSSN ..OVV''V'O termination model, and for the MEIS-optimised version of this model, compared with interlayer spacings in the best-fit half-metal and vanadyl terminations models, as described more fully in the text. All values are in Ångström units. The bracketed value was unspecified by the original authors and is therefore assumed to be bulk-like.

Parameter	KSA+ half-metal termination	relaxed vanadyl in. 1° misalignment	KSSN ..OVV''V'O	MEIS best-fit ..OVV''V'O
V_{top}=O	-	1.60	-	-
O_{top}-V_{top}	0.68	0.68	-	-
V'_{top}-O_{top}	0.93	0.98	0.86	0.91
V''_{top}-V'_{top}	-	-	0.19	0.18
V_2-V''_{top}	-	-	0.19	0.18
V_2-V'_{top}	0.35	0.36	-	-
O_2-V_2	1.02	0.98	0.99	0.98
V'_2-O_2	0.98	0.99	-	-
V_3-O_2	-	-	1.44	1.27
V_3-V'_2	0.36	0.36	-	-
O_3-V_3	0.98	0.98	1.06	0.98
V'_3-O_3	0.98	0.98	(0.98)	1.07

Figure Captions

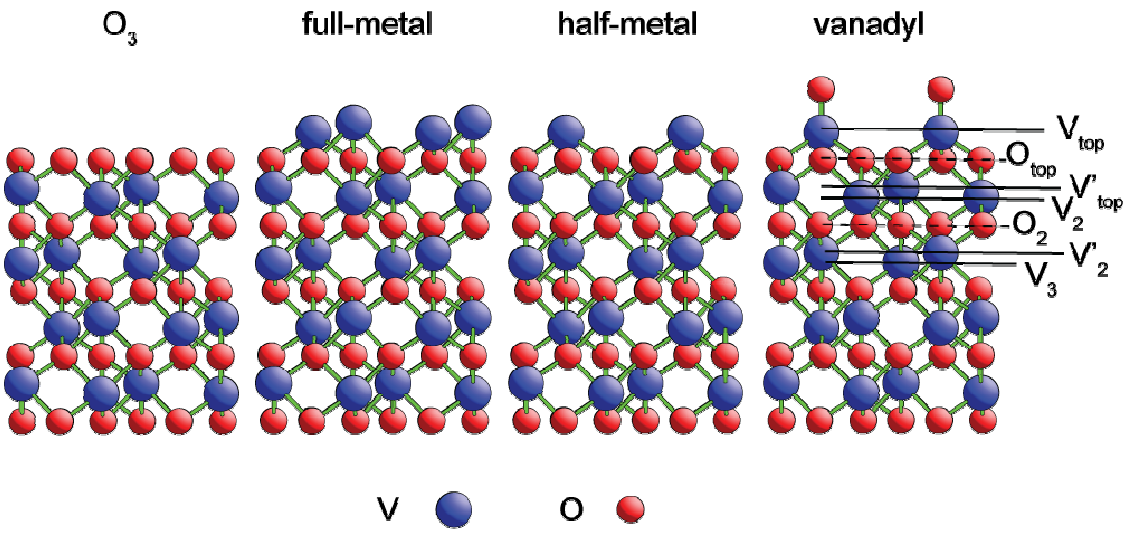

Fig. 1 Side views (viewed along $[2\bar{1}\bar{1}0]$) of $V_2O_3(0001)$, showing 4 possible surface terminations. The figure is drawn showing all interlayer spacings as in the bulk and thus does not include any surface relaxations. The nomenclature for referring to the outermost layers is shown on the right.

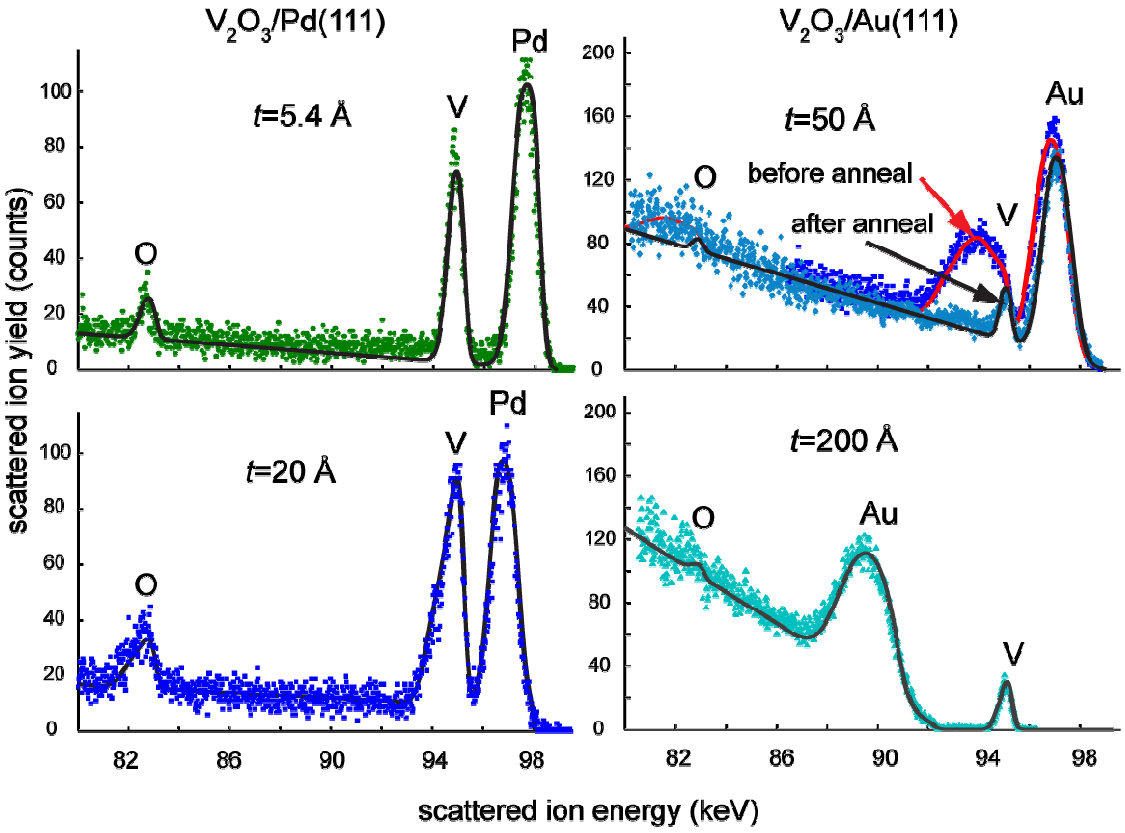

Fig. 2 Some scattered ion energy spectra for 100 keV H^+ ions incident on films of V_2O_3 grown in Pd(111) and Au(111), with different average thickness values, *t*. The data on the Pd substrate were recorded with $[\bar{1}10]$ incidence and [112] detection (parallel to $[\bar{4}22\bar{3}]$ and $[\bar{2}113]$, respectively, in the oxide); those on Au were obtained with $[00\bar{1}]$ incidence and [111] detection (parallel to $[8\bar{4}\bar{4}3]$ and [0001], respectively, in the oxide).

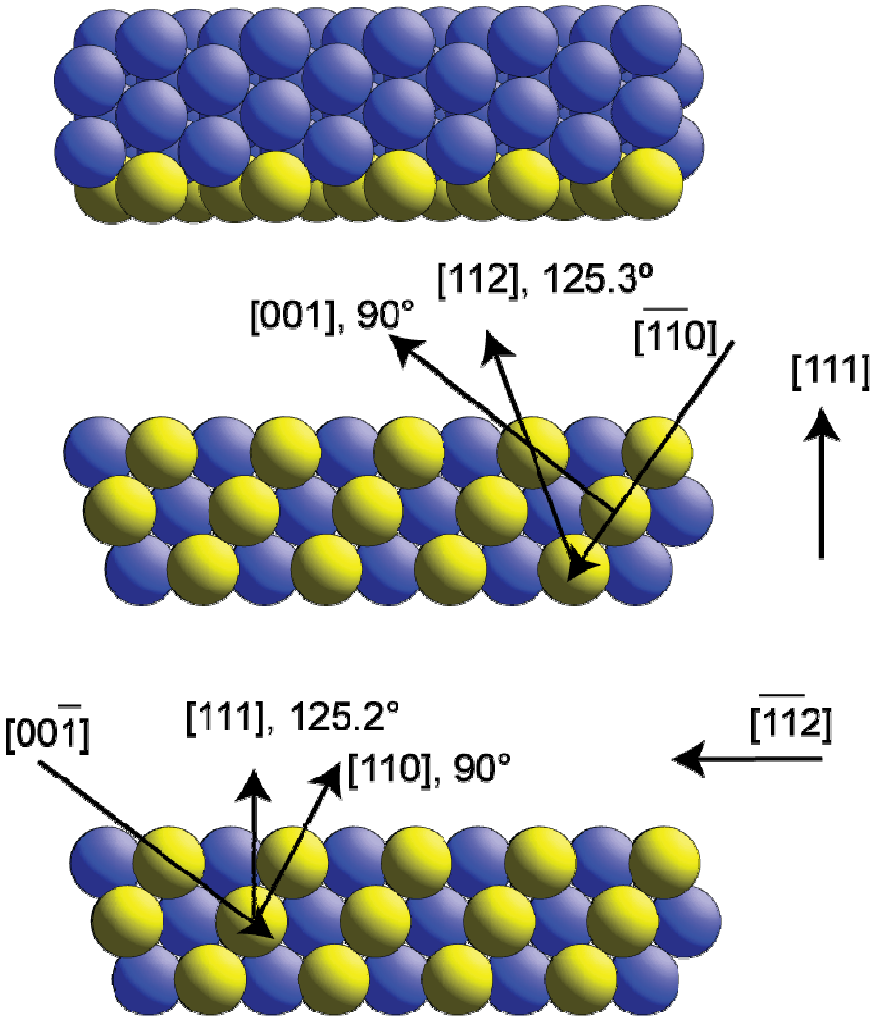

Fig. 3 Scattering geometries within the fcc (111) substrates used for the scattered ion energy spectra of Fig. 2. At the top is a plan view of the (111) surface with one scattering plane of atoms, perpendicular to the surface in the $[1\bar{1}2]$ azimuth shown with a lighter (yellow) shading. The lower diagrams show side views of this scattering plane with the incident and detection directions defined.

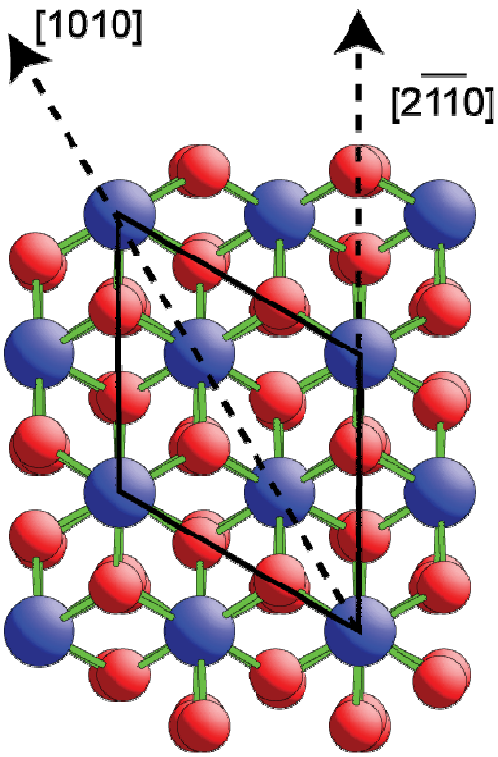

Fig. 4 Top view of the $V_2O_3(0001)$ surface (with a half-metal termination) including a definition of the two principle azimuths in which the MEIS experiments were conducted. The full lines show the surface unit mesh that is also the base of the hexagonal 3D unit cell.

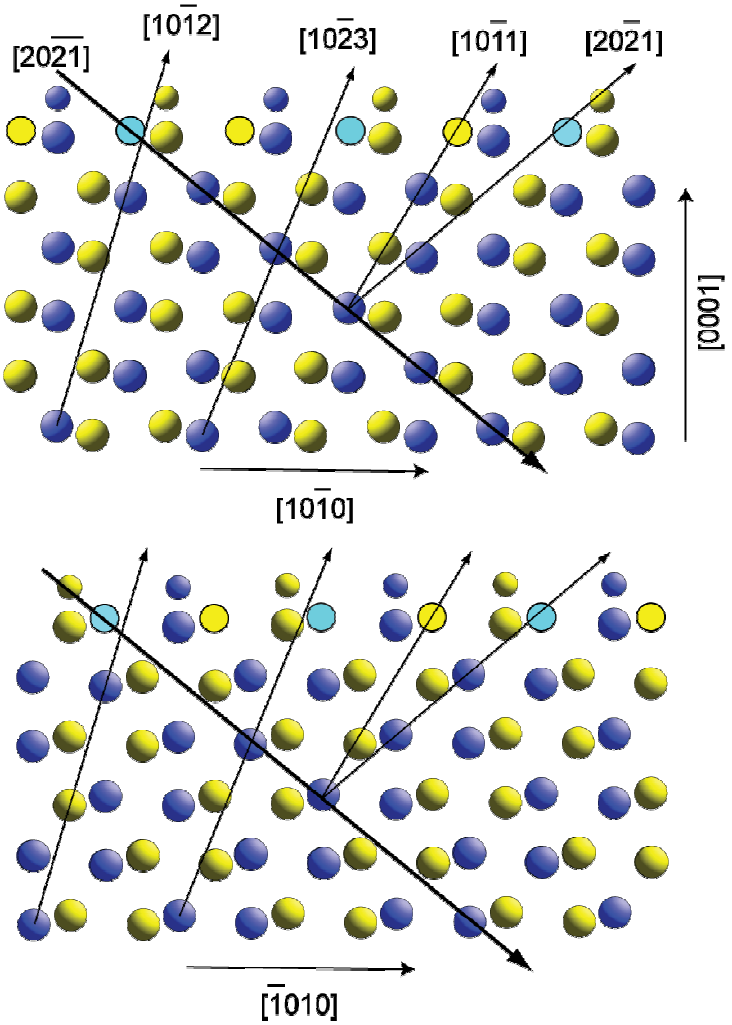

Fig. 5 The upper diagram shows a side view of the two inequivalent V scattering planes (shown in different colours) for V_2O_3 in the $[10\bar{1}0]$ azimuth, showing the incidence direction used and the main bulk blocking directions relevant to the measurement of the blocking curves in this azimuth. The lower diagram shows the structure of the alternative (180°) rotational domain, with the same directions marked. The diagram is shown for the vanadyl-terminated bulk structural model, the vanadyl O atoms being represented by the smaller shaded atoms at the top. The simple single-colour circles show the positions of the 'missing' outermost half-metal layer in this structure.

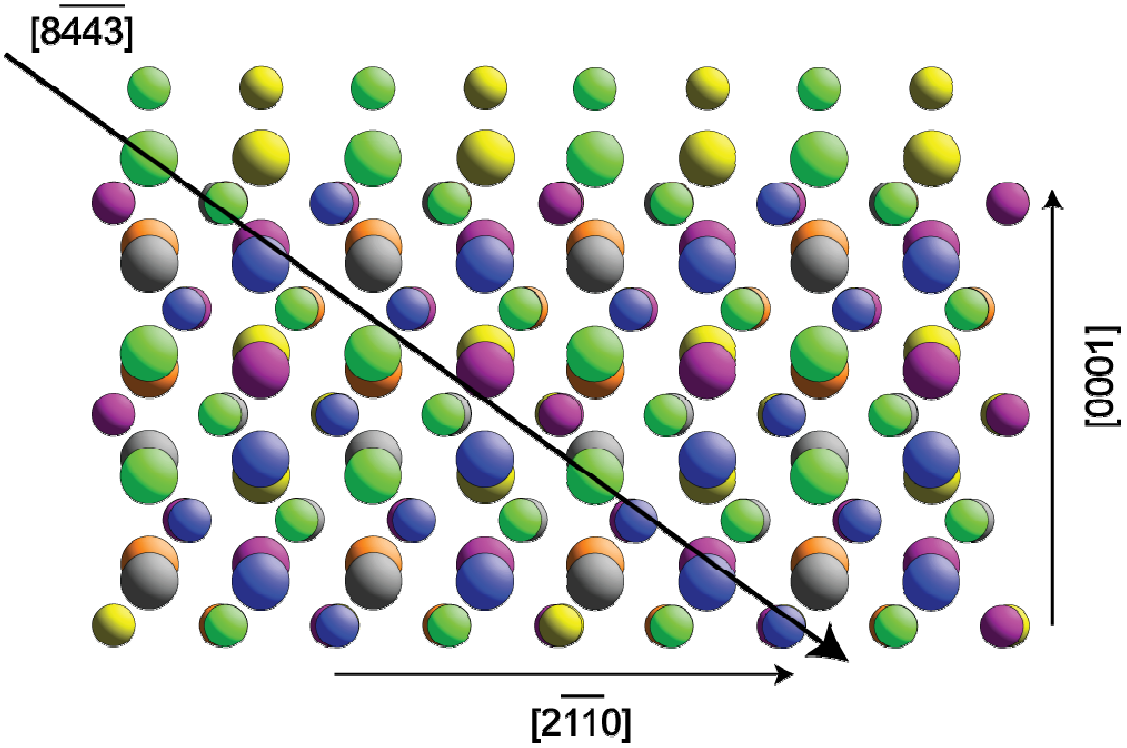

Fig. 6 Side view diagram of the four inequivalent V scattering planes (shown in different colours) for V_2O_3 in the $[2\bar{1}\bar{1}0]$ azimuth, showing the incidence direction used. Larger balls represent V atoms, smaller balls represent O atoms. The O atoms in the bulk lie slightly out of the V atom planes, but may be expected to produce some shadowing and blocking.

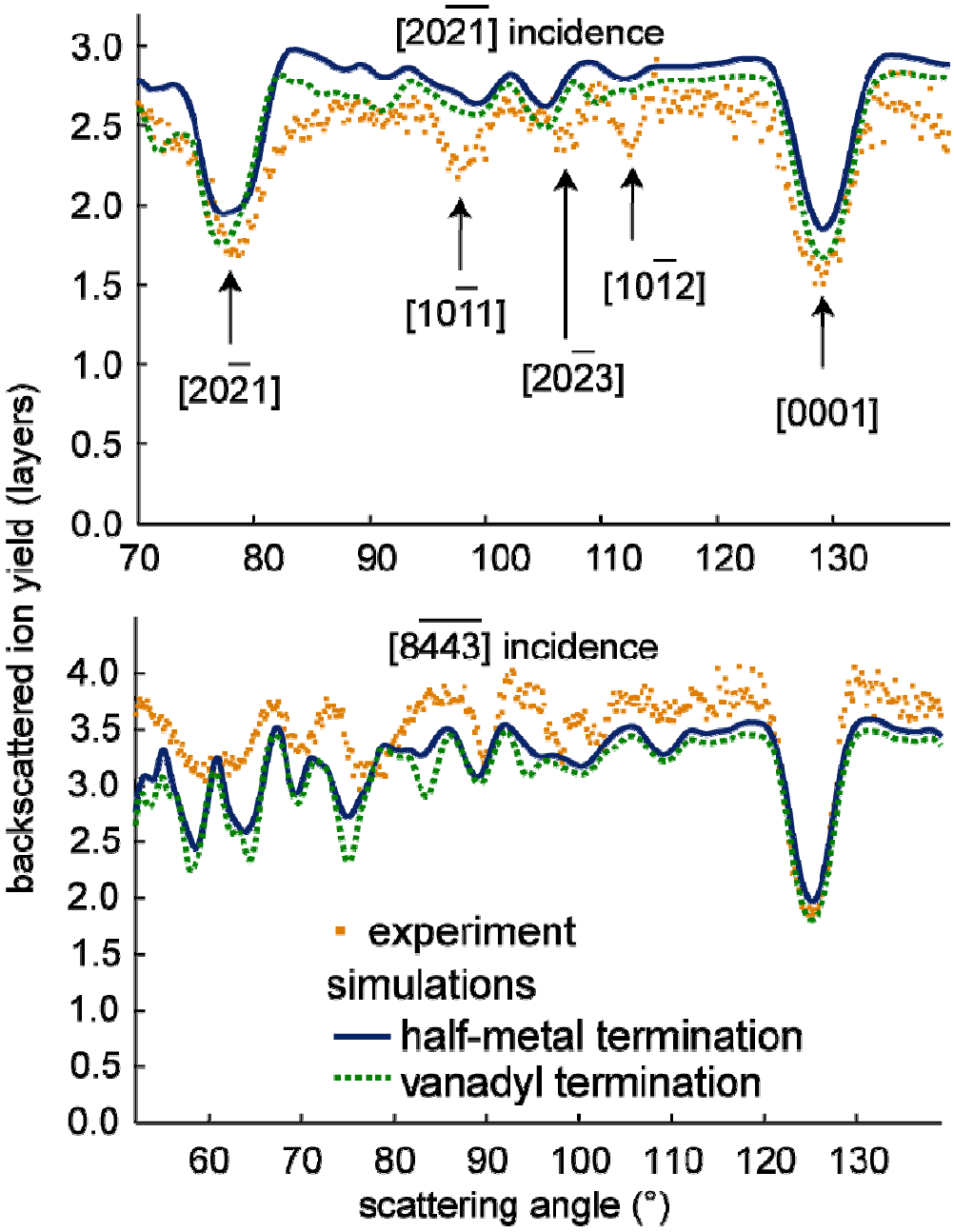

Fig. 7 Comparison of experimental 100 keV H^+ MEIS blocking curves from a 200 Å film of V_2O_3(0001)on Au(111) recorded in two different incidence directions with the results of VEGAS simulations for the half-metal and vanadyl termination models using the structural parameters values found in the earlier PhD experimental study (KSA+) [35].

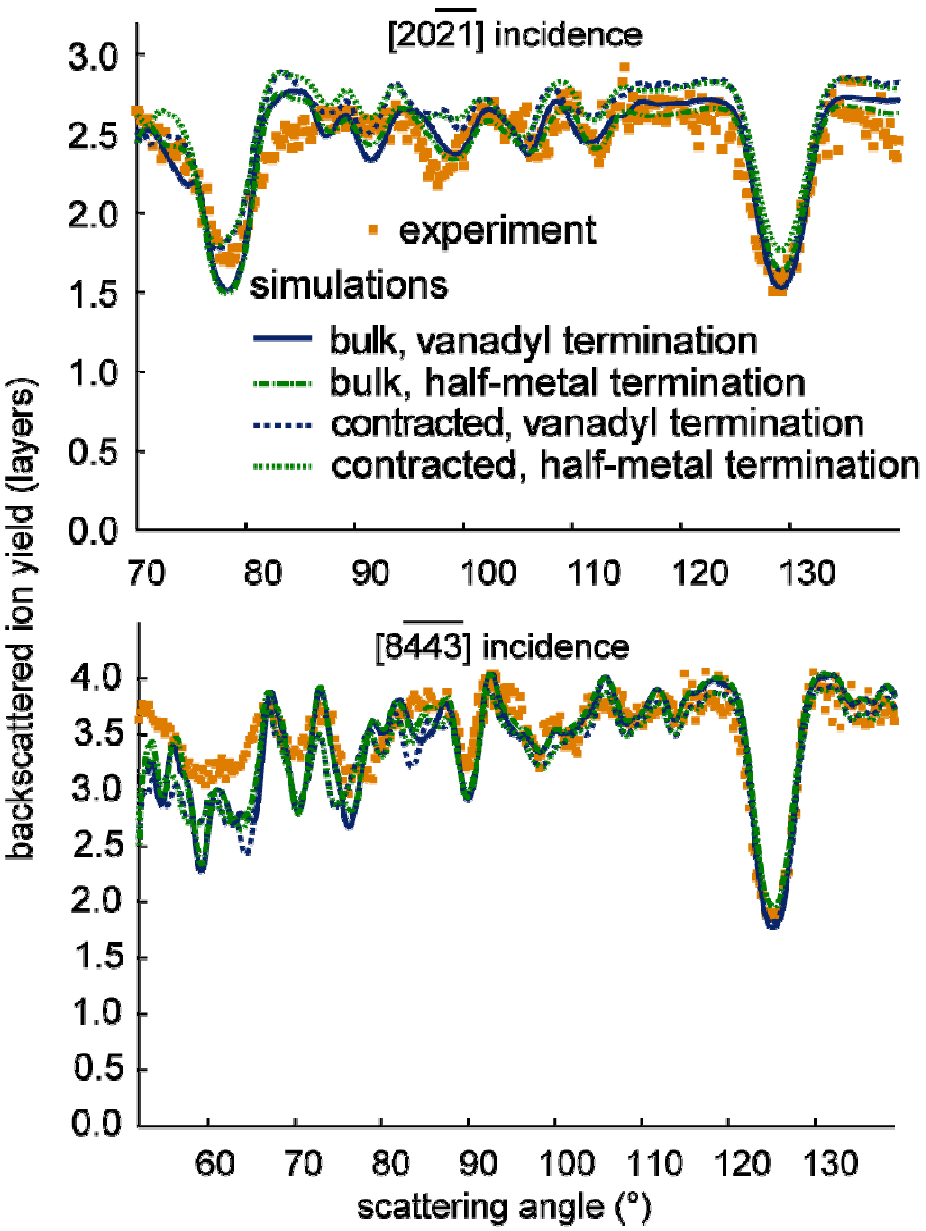

Fig. 8 Comparison of experimental 100 keV H^+ MEIS blocking curves from a 200 Å film of V_2O_3(0001)on Au(111) recorded in two different incidence directions with the results of VEGAS simulations for the half-metal and vanadyl termination models assuming a 1° misalignment of the incident direction. Results are shown for model both with and without surface relaxation.

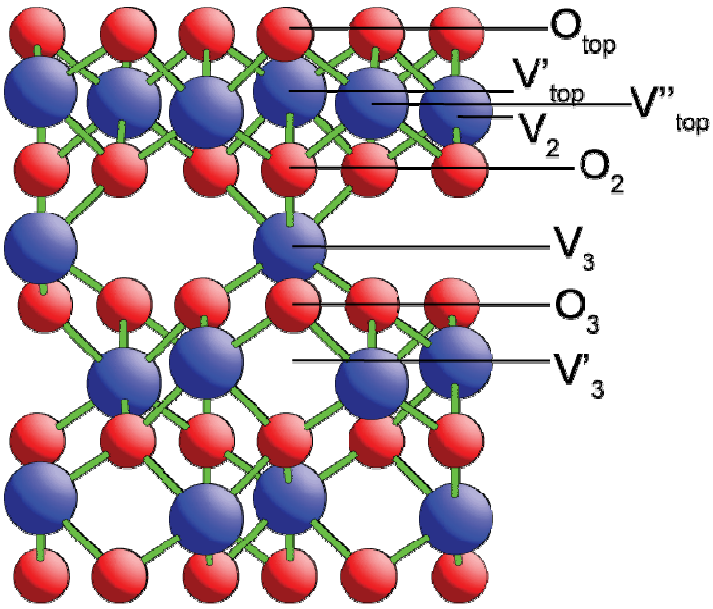

Fig. 9 Side view (viewed along $[2\bar{1}\bar{1}0]$) of $V_2O_3(0001)$, showing modified form of the oxygen termination (the KSSN ..VV''V'O model) in which the V'_2 half-metal layer moves up into the outermost buckled full metal layer (defined by the V'_{top} and V_2 half-layers) to become relabelled as V''top. The simplified model shown here has all other interlayer spacings as in the bulk.

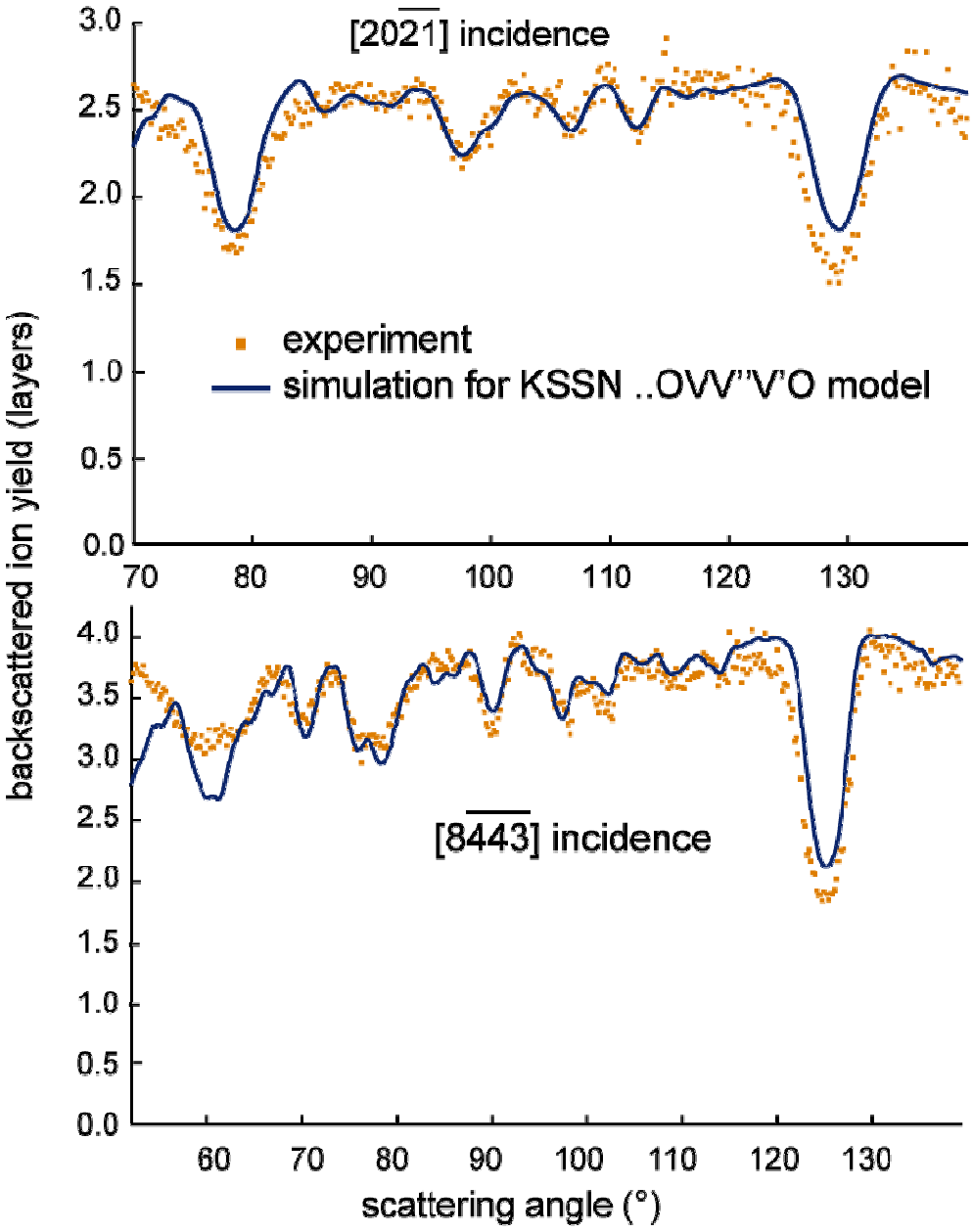

Fig. 10 Comparison of experimental 100 keV H^+ MEIS blocking curves from a 200 Å film of V_2O_3(0001)on Au(111) recorded in two different incidence directions with the results of VEGAS simulations for the optimised form of the KSSN ..OVV''V'O termination model shown schematically in Fig. 9.

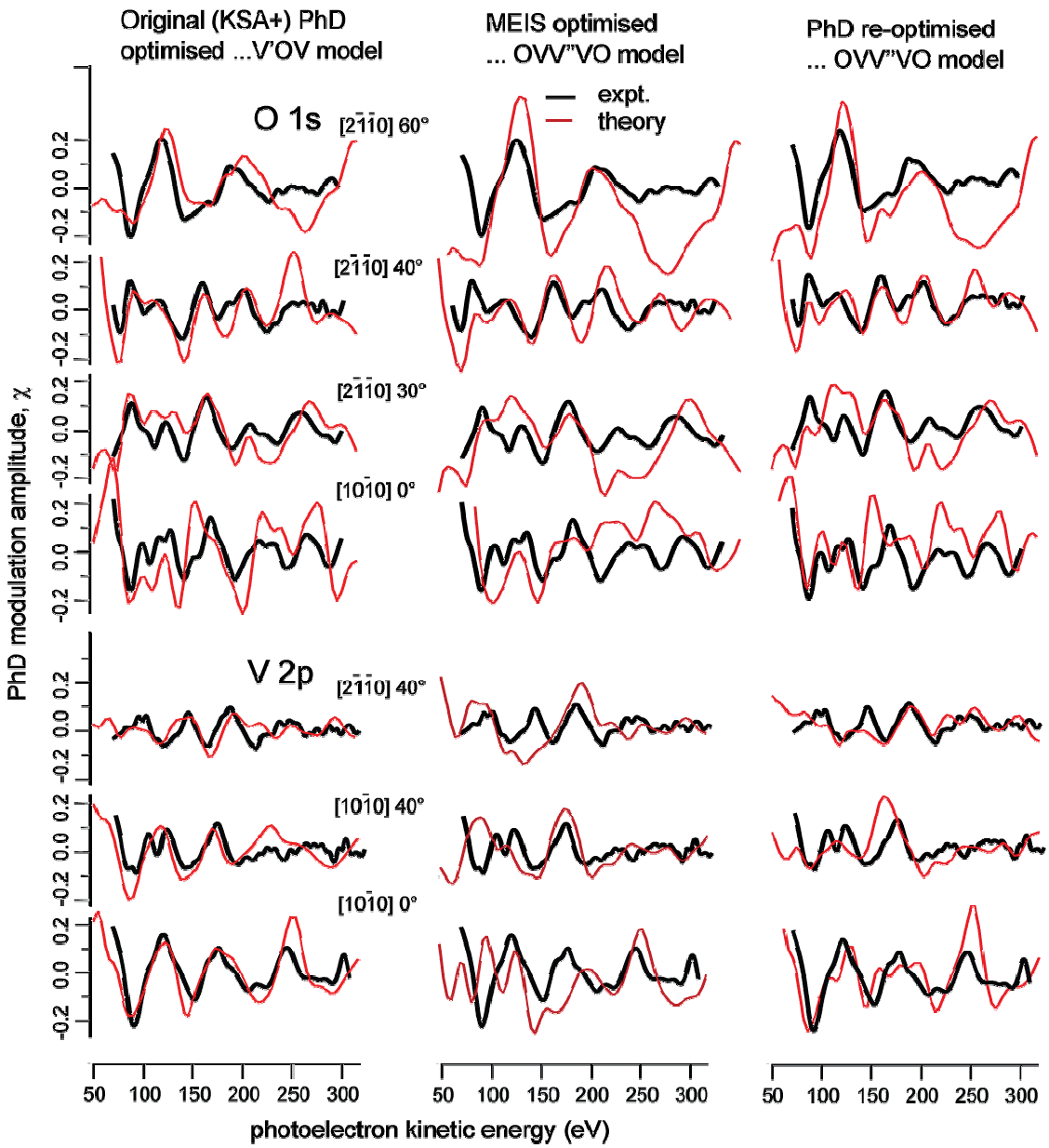

Fig. 11 Scanned energy mode photoelectron diffraction modulation spectra from KSA+ [35], showing the comparison with theoretical simulations for the original best-fit half-metal termination, and the new results for the MEIS-optimised, and PhD re-optimised, KSSN VO_2 termination models.

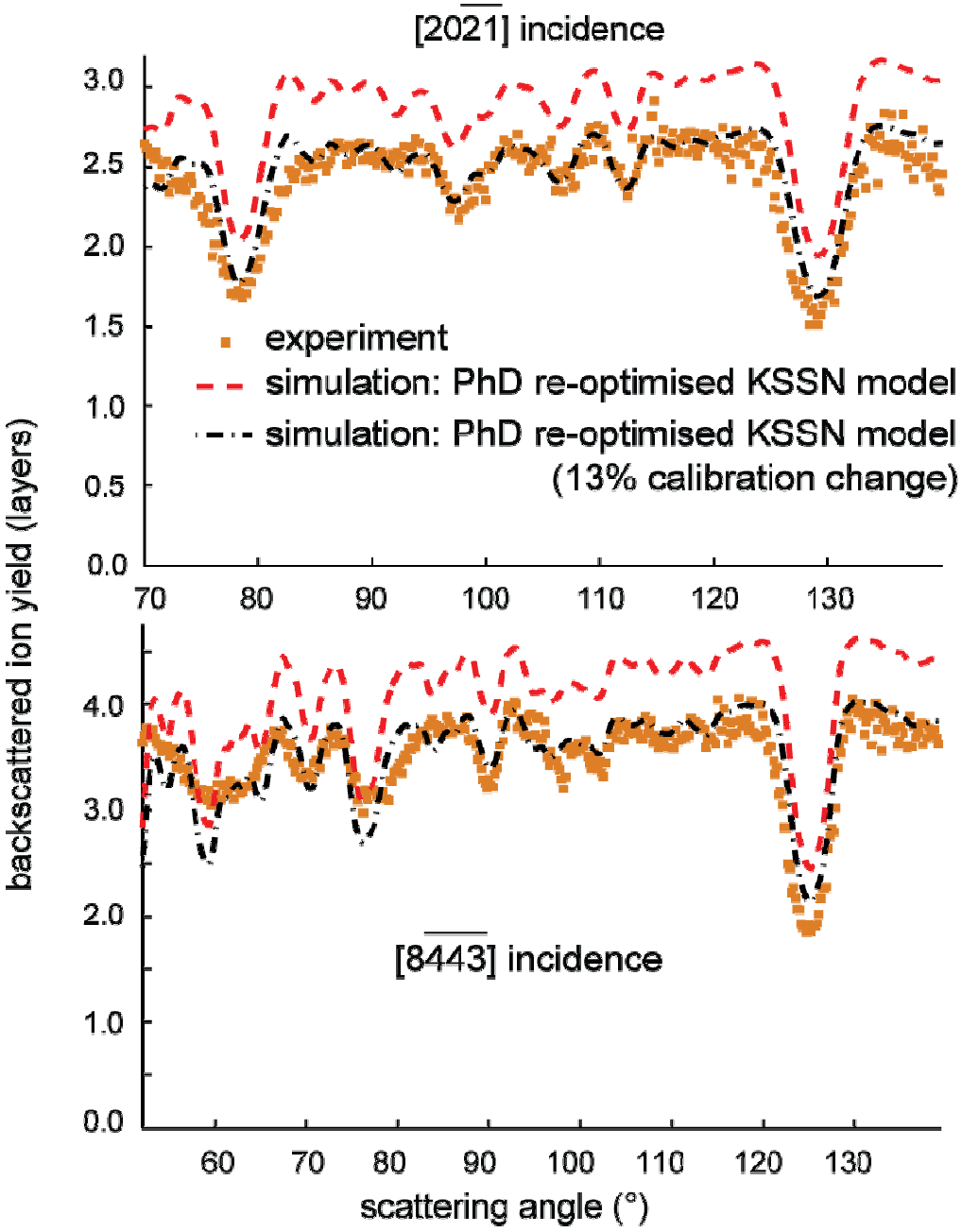

Fig. 12 Comparison of experimental 100 keV H^+ MEIS blocking curves from a 200 Å film of V_2O_3(0001)on Au(111) recorded in two different incidence directions with the results of VEGAS simulations for the PhD re-optimised variant of the KSSN ..OVV''V'O termination model, shown both without and with a change in the absolute calibration of the experimental ion yield scale.

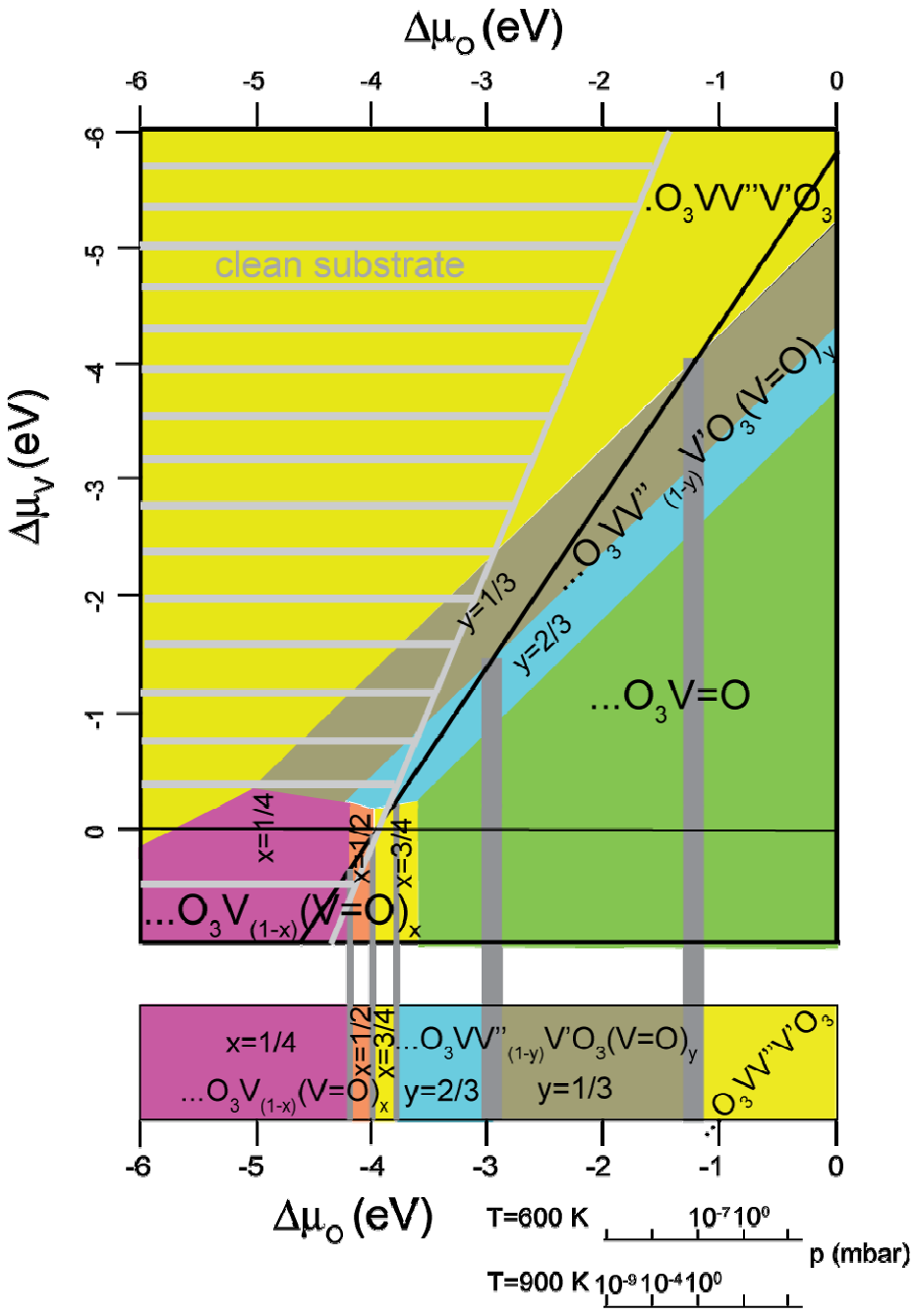

Fig. 13 Equilibrium phase diagram for the $V_2O_3(0001)$ surface as a function of relative oxygen and vanadium chemical potentials, adapted from the results of the calculations of TG-PS [32, 33], and described more fully in the text. At the bottom is a simplified diagram showing the different surface phase stability regions as a function of oxygen chemical potential, including corresponding oxygen partial pressures at two different temperatures.

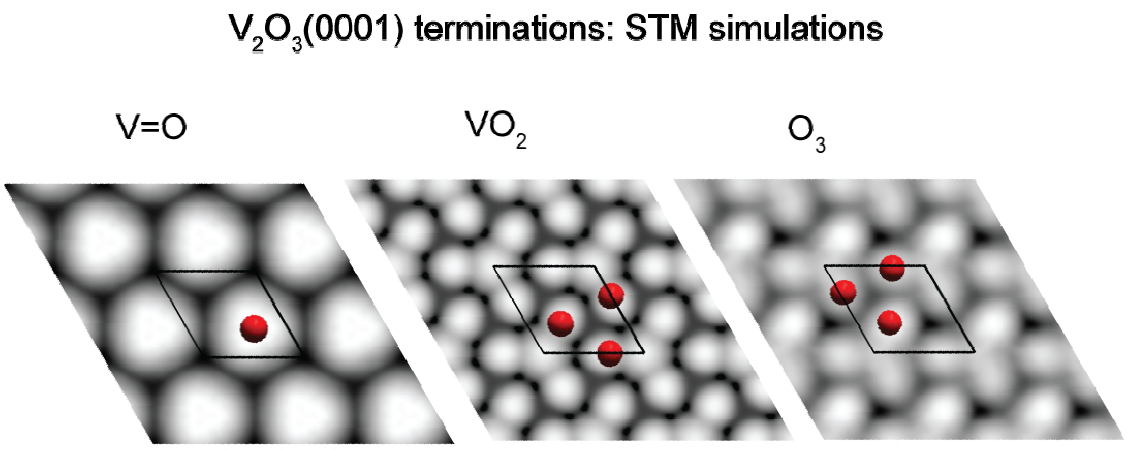

Fig. 14 Simulations of empty-state STM images from there different $V_2O_3(0001)$ terminations, vanadyl, reconstructed VO_2, and bulk O_3. The black rectangle shows a single surface unit mesh. The red circles correspond to the positions of the outermost O atoms in the surface.

References

1 B. Grzybowska-Świerkosz, F. Trifirò, J. C. Vedrine (eds) *Vanadia catalysts for selective oxidation of hydrocarbons and their derivatives*, Appl. Catal. A 157 (1997) 1.

2 C.F. Walters, K.F. McCarty, E.A. Soares, M.A. Van Hove, Surf. Sci. **464**, L732 (2000).

3 P. Guénard, G. Renaud, A. Barbier, M. Gautier-Soyer, Surf. Rev. Lett. **5**, 321 (1998).

4 R. Di Felice and J.E. Northrup, Phys. Rev. B **60**, 16287 (1999).

5 A. Rohrbach, J. Hafner, and G. Kresse, Phys. Rev. B **70**, 125426 (2004).

6 R. Rohr, M. Bäumer, H.-J. Fruend, J.A. Mejias, V. Staemmler, S. Müller, L. Hammer, K. Heinz, Surf. Sci. **372**, L291 (1997); erratum **389**, 391 (1997).

7 Th. Gloege, H.L. Meyerheim, W. Moritz, D. Wolf, Surf. Sci. **441**, L917 (1999).

8 M. Lübbe and W. Moritz, J. Phys.: Condens. Matter **21**, 134010 (2009).

9 O. Bikondoa, W. Moritz, X. Torrelles, H.J Kim, G. Thornton, R. Lindsay, Phys. Rev. B **81**, 205439 (2010).

10 A.J. Window, A. Hentz, D.C. Sheppard, G.S. Parkinson, H. Niehus, D. Ahlbehrendt, T.C.Q. Noakes, P. Bailey, D.P. Woodruff, Phys. Rev. Lett. 107 (2011) 016105.

11 G. Kresse, S. Surnev, J. Schoiswohl, F. P. Netzer, Surf. Sci. 555 (2004) 118.

12 A. –C. Dupuis, M. Abu Haija, B. Richter, H. Kuhlenbeck, H. –J. Freund, Surf. Sci. 539 (2003) 99.

13 S. Surnev, M. G. Ramsey, F. P. Netzer, Prog. Surf. Sci. **73** (2003) 117.

14 C. Kolczewski *et al.,* Surface Sci. **601**, 5394 (2007).

15 D. Göbke *et al.*, Angew. Chem. Int. Ed. **48**, 3695 (2009).

16 J.F. van der Veen, Surf. Sci. Rep. 5 (1985) 199

17 F. P. Leisenberger, S. Surnev, L. Vitali, M. G. Ramsey, F. P. Netzer, J. Vac. Sci. Technol. A 17 (1999) 1743.

18 S. Surnev, L. Vitali, M. G. Ramsey, F. P. Netzer, G. Kresse, J. Hafner, Phys. Rev. B 61 (2000) 13945.

19 S. Surnev, G. Kresse, M. G. Ramsey, F. P. Netzer, Phys. Rev. Lett. 87 (2001) 86102.

20 S. Surnev, G. Kresse, M. Sock, M. G. Ramsey, F. P. Netzer, Surf. Sci. 495 (2001) 91.

21 C. Klein, G. Kresse, S. Surnev, F. P. Netzer, M. Schmid, P. Varga, Phys. Rev. B 68 (2003) 235416.

22 J. Schoiswohl, M. Sock, S. Surnev, M.G. Ramsey, F.P. Netzer, G. Kresse, J.N. Andersen, Surf. Sci. 555 (2004) 101.

23 H. Niehus, R. P. Blum, D. Ahlbehrendt, Physica Status Solidi **A 187** (2001) 151.

24 H. Niehus, R. -P. Blum, D. Ahlbehrendt,Surf. Rev. Lett., 10 (2003) 353 .

25 J. Schoiswohl, M. Sock, S. Eck, S. Surnev, M. G. Ramsey, F. P. Netzer, Phys. Rev. B 69 (2004) 155403.

26 J. Schoiswohl, M. Sock, S. Surnev, M. G. Ramsey, F. P. Netzer, G. Kresse, J. N. Andersen, Surf. Sci. 555 (2004) 101.

27 F. Pfuner, J. Schoiswohl, M. Sock, S. Surnev, M. G. Ramsey, F. P. Netzer, J. Phys.: Condens. Matter 17 (2005) 4035.

28 P. D. Dernier, J. Phys. Chem. Solids 31 (1970) 2569.

29 I. Czekaj, K. Hermann, M. Witko, Surf. Sci. 525 (2003) 33.

30 I. Czekaj, M. Witko, K. Hermann, Surf. Sci. 525 (2003) 46.

31 I. Czekaj, K. Hermann, M. Witko, Surf. Sci. 545 (2003) 85.

32 T. K. Todorova, M. V. Ganduglia-Pirovano, J. Sauer, J. Phys. Chem. **B 109** (2005) 23523.

33 T. K. Todorova, M. V. Ganduglia-Pirovano, J. Sauer, J. Phys. Chem. **C 111** (2007) 5141

34 C. Kolczewski, K. Hermann, S. Guimond, H. Kuhlenbeck, H. –J. Freund, Surface Sci. 601 (2007) 5394.

35 E. A. Kröger, D. I. Sayago, F. Allegretti, M. J. Knight, M. Polcik, W. Unterberger, T. J. Lerotholi, K. A. Hogan, C. L. A. Lamont, D. P. Woodruff, Surf. Sci. 601 (2007) 3350.

36 Y. Romanyshyn, H. Kuhlenbeck, H. –J. Freund, to be published.

37 P. Bailey, T.C.Q. Noakes, D.P. Woodruff, Surf. Sci. 426 (1999) 358

38 R.M. Tromp, M. Copel, M.C. Reuter, M. Horn von Hoegen, J. Speidell and R. Koudijs, Rev. Sci. Instrum. 62, 2679 (1991)

39 D. Brown, T.C.Q. Noakes, D.P. Woodruff, P. Bailey and Y. Le Goaziou, J. Phys.: Condens. Matter 11 (1999) 1889

40 M. Mayer, http://www.rzg.mpg.de/~mam/index.html. *SIMNRA Program.*

41 J. F. Ziegler, www.srim.org.

42 R.M. Tromp, J.F. van der Veen, Surf. Sci. 133 (1983) 159

43 T.C.Q. Noakes, P. Bailey, D.P. Woodruff, Nucl. Instrum. Methods B 136 (1998) 1125

44 D.P. Woodruff, D. Brown, P.D. Quinn, T.C.Q. Noakes, P. Bailey, Nucl. Instrum. Methods B 183 (2001) 128

45 H. Kuhlenbeck, private communication

46 J. Seifert, E. Meyer, H. Winter, H. Kuhlenbeck, Surf. Sci. 606 (2012) L41

47 J.P. Perdew, J.A. Chevary, S.H. Vosko, K.A. Jackson, M.R. Pederson, D.J. Singh, C. Fiolhais,. Phys. Rev. B 46 (1992) 6671.

48 Y. Romanyshn, S. Guimond, H. Kuhlenbeck, S. Kaya, R.P. Blum, H. Niehus, S. Shaikhutdinov, V. Simic-Milosevic, N. Nilius, H.-J. Freund, M.V. Ganduglia-Pironavo, R. Fortrie, J. Döbler, J. Sauer, Top. Catal. 50 (208) 106.

49 M Abu Haija, S, Guimond, A. Uhl, H. Kuhlenbeck, H.-J. Freund, Surf. Sci. 600 (2006) 1040.

50 M Abu Haija, S, Guimond, Y. Romanyshyn,A. Uhl, H. Kuhlenbeck, T.K. Todorova, M.V. Ganduglia-Pirovano, J. Döbler, J. Sauer, H.-J. Freund, Surf. Sci. 600 (2006) 1497.

51 E. A. Kröger, D. I. Sayago, F. Allegretti, M. J. Knight, M. Polcik, W. Unterberger, T. J. Lerotholi, K. A. Hogan, C. L. A. Lamont, M. Cavalleri, K. Hermann, D. P. Woodruff, Surf. Sci. 602 (2008) 1267